Ocean Engineering 340 (2025) 122279

Contents lists available at ScienceDirect

Ocean Engineering

journal homepage: www.elsevier.com/locate/oceaneng

Research paper

# The sound source distribution and mechanisms of flow-sound correlation for cavitating propellers

Lianjie Yu [a], Decheng Wan [b,*], Yan Gao [a], Qi Shen [a], Shang Shi [a], Jiaao Geng [a]

[a] China Ship Scientific Research Center, Wuxi, China
[b] Computational Marine Hydrodynamic Lab (CMHL), School of Naval Architecture, Ocean and Civil Engineering, Shanghai Jiao Tong University, Shanghai, China

ARTICLE INFO

*Keywords:*
Hydrodynamics
Flow-sound correlation
underwater noise
Acoustic analogy

ABSTRACT

Cavitating propeller is a main underwater sound source in ocean engineering. Its sound source distribution and flow-sound correlation mechanism are of interest for scholars. In this paper, four source components are considered. Large eddy simulation and acoustic analogy are adopted for flow-sound correlation mechanism study. Taking INSEAN E779A propeller as the research object, the predicted noise is compared with the experiments. It is found that the error is less than 6 dB. The correlation between the propeller side force and the dipole sound is high in all frequency bands. The lower the cavitation number, the higher the surface force fluctuation, which is reflected in the increased dipole intensity. The vortex affects the turbulence in the wake region, which contributes to the quadrupole source. The cavitation behavior affects the sphere pressure. The smaller the cavitation number and the larger the std value of the cavitation area, the stronger the sphere source is. The monopole, dipole and quadrupole sound components under non-uniform inflow conditions all exhibit more pronounced narrow-band peaks than those of uniform inflow. DMD results of the propeller wake vortices reveals that the uniform inflow, despite its higher energy at the 1st order mode, decays rapidly at higher order modes, while the non-uniform inflow decays slower, resulting in more pronounced peaks at the higher order frequencies.

## 1. Introduction

Propeller is an important noise source in many engineering scenarios (Posa et al., 2022). It is easy to induce cavitation at high rotation speeds, which makes cavitating propeller noise a hot issue. The shape of propeller is complex. It has three-dimensional deformation, and its flow is affected by the incoming velocity, cavitation number, non-uniformity and other factors. Since propellers are widely used in the ocean engineering, its noise prediction research also has more significance.

Propeller cavitation noise is classified into 2 categories: open water propeller noise (uniform incoming flow) and wake flow propeller noise (non-uniform incoming flow). For open water case, it was found that cavitation increases the sound level in all frequency bands (Lidtke et al., 2016). It has been demonstrated that propeller cavitation leads to an increase in the total sound pressure level at least 7 dB (Zhu et al., 2017). When blade cavitation and hub cavitation all occur, the sound pressure level increases at least 10 dB. This is an effect that should not be ignored when compared to other noise sources (e.g., mechanical noise) on a ship (Noughabi et al., 2017). Experimentally, some scholars [148] summarized some semi-empirical formulas for the fast prediction of propeller cavitation noise (Bosschers, 2018), but the analysis of the flow-acoustic correlation could not be performed. The difficulty of real-scale measurements highlights the urgency of the development of numerical prediction solvers for cavitation noise.

For the computational prediction methods for radiated noise, many researchers have used the acoustic analogy to predict hydrodynamic noise of propellers (Sezen and Kinaci, 2019). However, the current research focuses mainly on the monopole and dipole sound pressure. Even if the quadrupole is considered, the porous integral surface is considered sensitive and inaccurate (Cianferra et al., 2019). Under cavitation conditions, there is no research that considers both the quadrupole volume integration and the sphere sound pressure of the propeller. The influence of the sound source distribution characteristics and flow-sound correlation mechanisms of cavitating propellers are still unknown.

In this paper, INSEAN E779A four-bladed propeller is selected as the research object to analyze the flow-acoustic correlation mechanism. Propeller lateral force, vortex shedding, cavitation, and non-

* Corresponding author.
*E-mail address:* dcwan@sjtu.edu.cn (D. Wan).

https://doi.org/10.1016/j.oceaneng.2025.122279
Received 24 December 2024; Received in revised form 15 June 2025; Accepted 21 July 2025

**Table 1**
The geometry information of INSEAN E779A propeller.

| INSEAN E779A | |
|---|---|
| Disk surface diameter D (m) | 0.22727 |
| Number of blades | 4 |
| Pitch angle (°) | 4° 35' (forward) |
| Skew angle (°) | 4° 48' (right-handed) |
| Pitch ratio | 1.1 |
| Disk area ratio ($A_e$/ $A_o$) | 0.689 |

homogeneous incoming flow are studied in the sound source distribution of various types. Experimental comparisons are made in non-uniform incoming conditions so as to verify the reliability for propeller noise prediction. Sound source mapping, dual grid technique, the third-generation vortex identification technique, and DMD analysis are shown in the paper to complete the research on the flow-acoustic correlation analysis for cavitation propeller.

## 2. Mathematical foundation

### 2.1. Large eddy simulation

There are two ways for solving N-S equation: One is decoupling in time remaining time-averaged pressure and random pressure; The other is decoupling in space remaining large-scale pressure and sub-grid-scale (SGS) pressure. The former is called RANS (Reynolds Averaged N-S Simulation), and the letter is called LES (Large Eddy Simulation). As RANS is focused on time-averaged quantities, it seems not suitable for noise prediction. LES is better for hydroacoustic study.

If external force is ignored, after space filtering, N-S equation is written

$$\frac{\partial \widetilde{u_i}}{\partial t}+\frac{\partial\left(\widetilde{u_i u_j}\right)}{\partial x_j}=-\frac{1}{\rho}\frac{\partial \widetilde{p}}{\partial x_i}+\nu\nabla^2\widetilde{u_i}$$

where superscript $\sim$ means the quantity is filtered in space. $u_i, u_j$ is velocity in different directions with $i,j = 1,2,3$. $p$ is pressure underwater. $\rho$ stands for density whose value is 1000kg/m$^3$. $\nu$ is kinematic viscosity whose value is $1\times10^{-3}$m$^{-1}$. Here, $\widetilde{u_i u_j}$ can be split by $\widetilde{u_i}\widetilde{u_j}$ and $\widetilde{u_i u_j}-\widetilde{u_i}\widetilde{u_j}$. The former indicates the momentum transportation among quantities after space filtering, and the latter indicates the momentum transportation between quantities after space filtering and SGS quantities. For convenience, $\tau^{SGS}=\widetilde{u_i u_j}-\widetilde{u_i}\widetilde{u_j}$ is named as SGS stress tensor. Therefore, the filtered N-S equation is written as:

$$\frac{\partial \widetilde{u_i}}{\partial t}+\frac{\partial\left(\widetilde{u_i}\widetilde{u_j}\right)}{\partial x_j}=-\frac{1}{\rho}\frac{\partial \widetilde{p}}{\partial x_i}+\nu\nabla^2\widetilde{u_i}+\nabla\cdot\tau^{SGS}$$

Like turbulence model in RANS, SGS model is introduced in LES for closure. According to Eddy-viscosity theory,

$$\tau^{SGS}=\frac{2}{3}\mathrm{tr}(\widetilde{S})\mathrm{I}-2\nu_{SGS}\widetilde{S}$$

where $\widetilde{S}$ is the spatial derivative of velocity. I is identity matrix, and tr( ) means the leading diagonal of matrix. $\nu_{SGS}$ is viscosity in SGS, which is expressed in different ways. In the original Smogorinsky model (Smagorinsky, 1963), there is

$$\nu_{SGS}=\left(C_S\Delta\right)^2\left(\widetilde{S}_{ij}\widetilde{S}_{ij}\right)^{1/2}$$

Here, $\Delta$ is the filter scale. $C_S\Delta$ can be seen as mixing length. $C_S$ is named as Smagorinsky constant, which is around 0.18 according to experiment results.

However, there is a drawback for Smogorinsky model, that is $\nu_{SGS}\neq 0$ near the walls. In order to solve this problem, WALE model (Wall-Adapting Local Eddy) is proposed (Nicoud and Ducros, 1999), which allows to adopt a damping factor adapting the distance from walls, like

$$\nu_{SGS}=\left(\frac{C_w^2\Delta}{C_k}\right)^2\frac{\left(\widetilde{S}_{ij}\widetilde{S}_{ij}\right)^3}{\left(\left(\widetilde{S}_{ij}\widetilde{S}_{ij}\right)^{5/2}+\left(\widetilde{S}_{ij}\widetilde{S}_{ij}\right)^{5/4}\right)^2}$$

Where $C_w$ and $C_k$ are constant factors according to experiments. WALE is proved more accurate than Smogorinsky in literatures (Zhao et al., 2023). Therefore, WALE SGS model is adopted in this paper.

**Table 2**
The cavitation condition settings of INSEAN E779A propeller.

| Number | $J$ | $\sigma_n$ | $U_0$ (m/s) | $n$ (rps) |
|---|---|---|---|---|
| NO.1 | 0.710 | 0.630 | 5.808 | 35.99 |
| NO.2 | 0.710 | 1.007 | 5.813 | 36.01 |
| NO.3 | 0.710 | 1.763 | 5.809 | 36.02 |
| NO.4 | 0.770 | 1.042 | 6.224 | 35.61 |
| NO.5 | 0.830 | 1.029 | 6.716 | 35.61 |
| NO.6 | – | – | 6.220 | 30.50 |

*where $J=\frac{U_0}{nD}$, $\sigma_n=\frac{p_\infty-p_v}{\frac{1}{2}\rho(nD)^2}$. $U_0$ is the inlet velocity. $n$ is rotation speed. $p_\infty$ is the pressure at outlet plane.


**Fig. 2.** The artificial non-uniform wake generator for INSEAN E779A propeller.

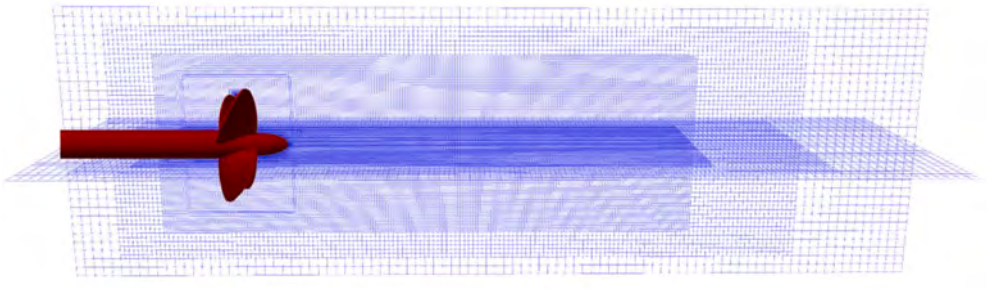

**Fig. 1.** General view of the grid structure (Coarse grid): Unstructured grid is used around propeller; Structured grid is used in the far field.

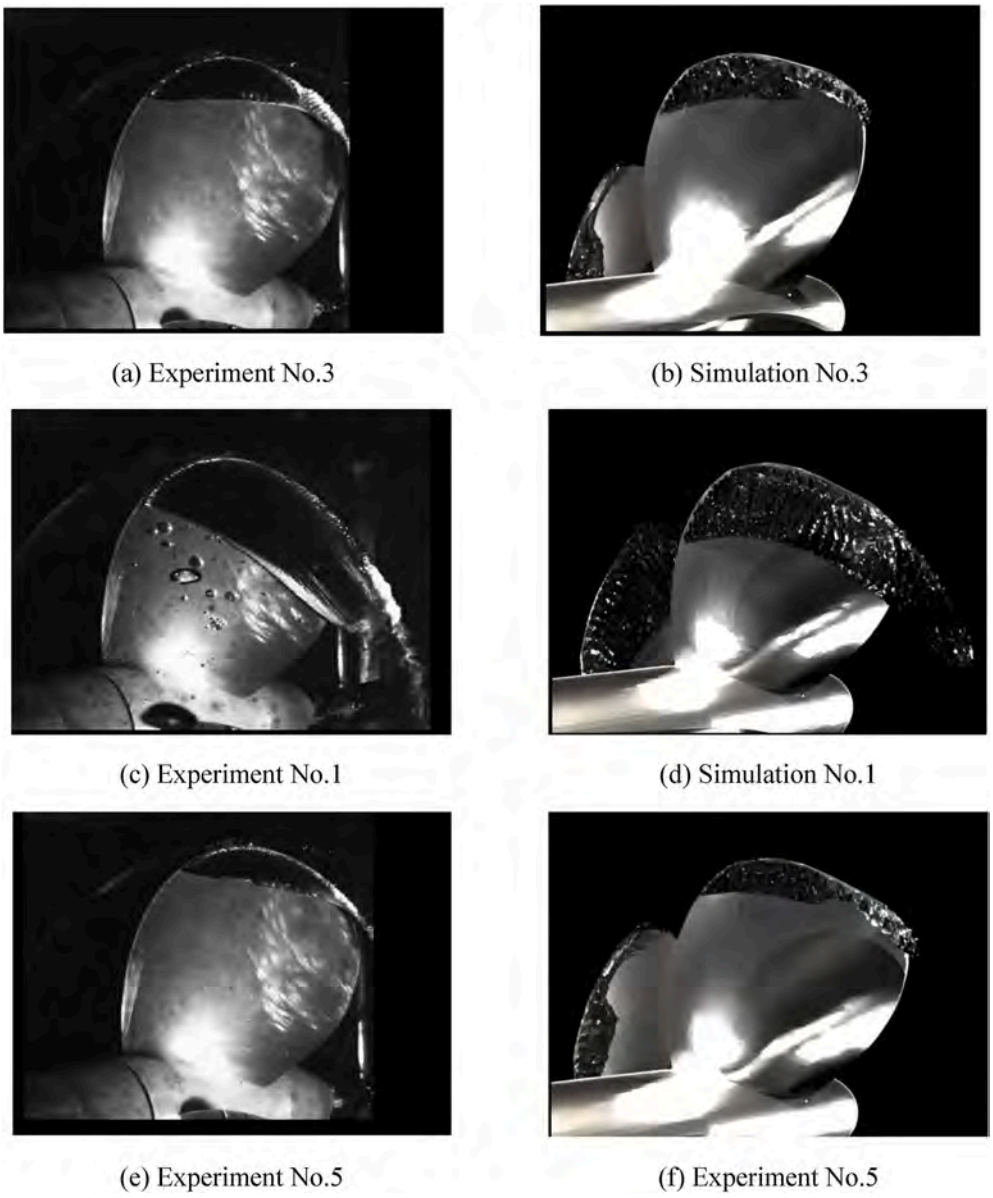


**Fig. 3.** The cavitation pictures compared with experiments for uniform velocity.

**Table 3**
The error of cavitation area of INSEAN E779A propeller for uniform velocity.

| Condition | $J$ | $\sigma_n$ | $\overline{A}_c/A_0$ | Exp. | Error | $\widehat{A}_c/A_0$ | Exp. | Error |
|---|---|---|---|---|---|---|---|---|
| NO.1 | 0.710 | 0.63 | 0.379 | 0.387 | 2.07 % | 1.416 | 1.308 | 8.26 % |
| NO.2 | 0.710 | $\approx 1.03$ | 0.260 | 0.268 | 2.99 % | 0.809 | 0.791 | 2.28 % |
| NO.3 | 0.710 | 1.763 | 0.125 | 0.120 | 4.17 % | 0.269 | 0.254 | 5.91 % |
| NO.4 | 0.770 | $\approx 1.03$ | 0.201 | 0.188 | 6.91 % | 0.988 | 0.956 | 3.35 % |
| NO.5 | 0.830 | $\approx 1.03$ | 0.102 | 0.099 | 3.03 % | 0.420 | 0.402 | 4.48 % |

*where $A_0 = 0.115D^2$, $A_c$ stands for cavitation area.

### 2.2. Cavitation model

Cavitation is an own issue for underwater environment. Its simulation should consider two additional equations except for N-S equation: state equation and cavitation mass transport equation.

The state equation contains two process: vaporation and condensation.

$$\frac{\partial \alpha_l \rho_l}{\partial t} + \nabla \cdot \left( \alpha_l \rho_l \overrightarrow{u}_l \right) = \dot{m}$$

$$\frac{\partial \alpha_v \rho_v}{\partial t} + \nabla \cdot \left( \alpha_v \rho_v \overrightarrow{u}_v \right) = -\dot{m}$$

The subscript '$l$' means liquid quantities, while '$v$' means vapor quantities. $\alpha$ is volume fraction and there is $\alpha_l = 1 - \alpha_v$. $\overrightarrow{u}$ is velocity

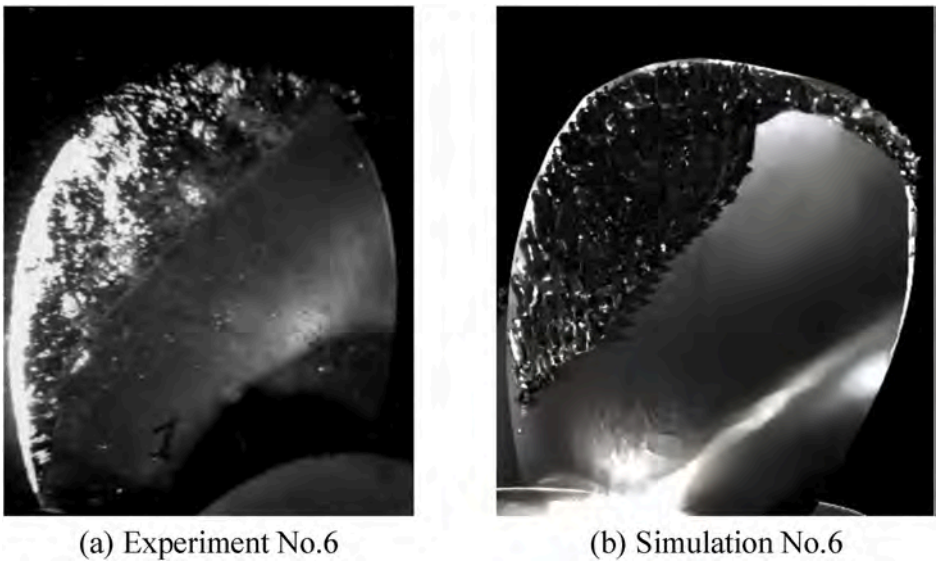


**Fig. 4.** The cavity snapshot compared with experiment in non-uniform wake.

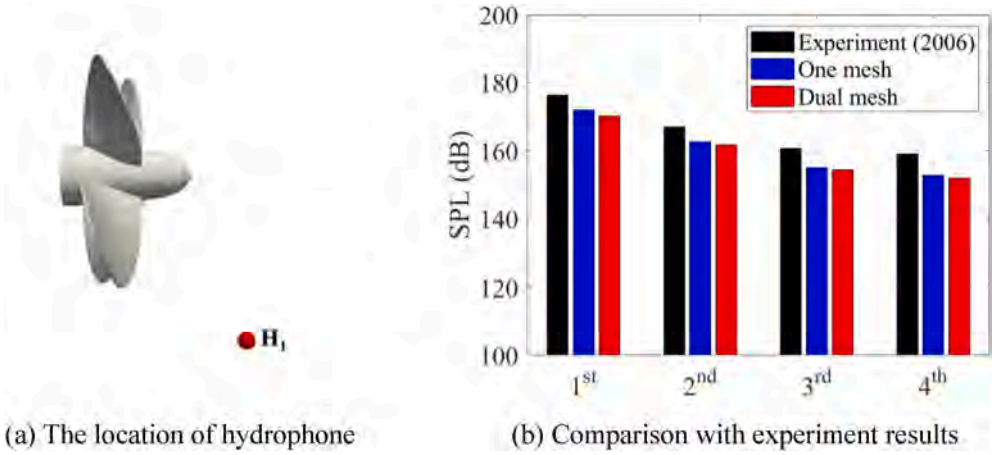


**Fig. 5.** The cavity snapshot compared with experiment in non-uniform wake.

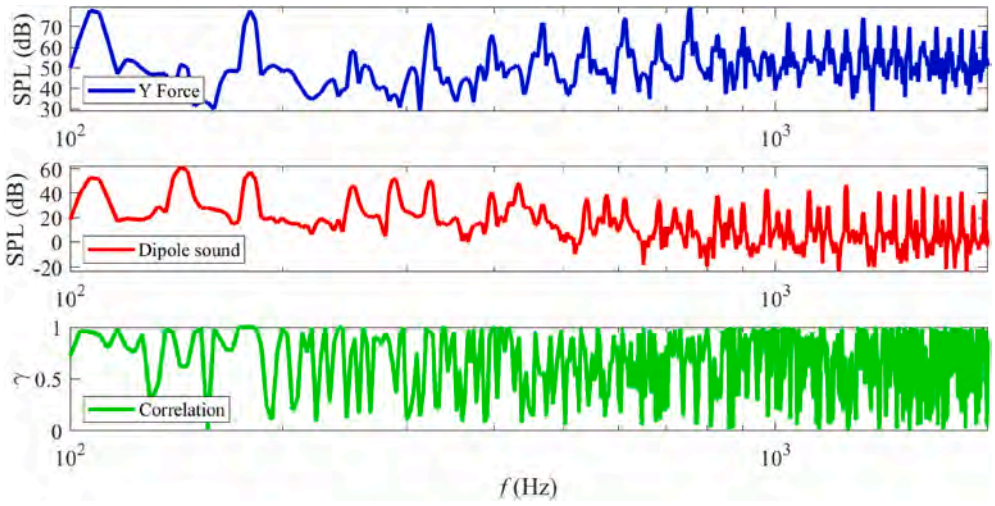


**Fig. 6.** The correlation between dipole sound and side force for NO.2 case.

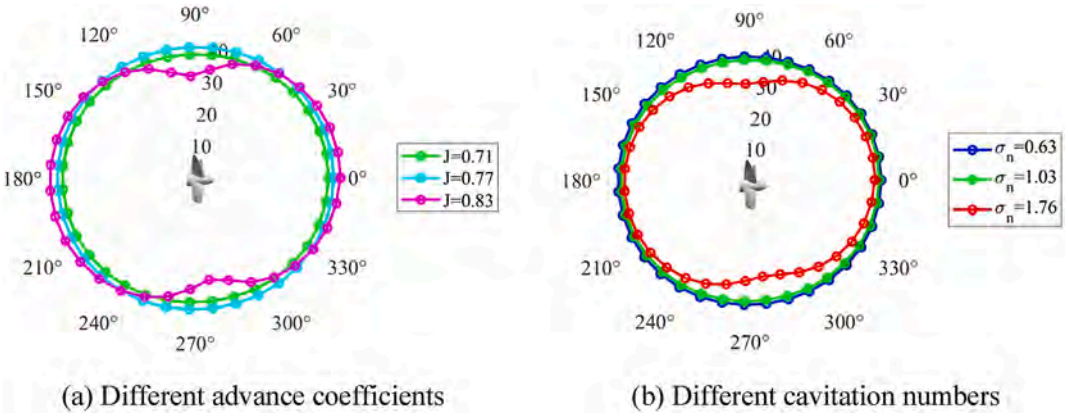


**Fig. 7.** The sound directivity of monopole and dipole results in different conditions.

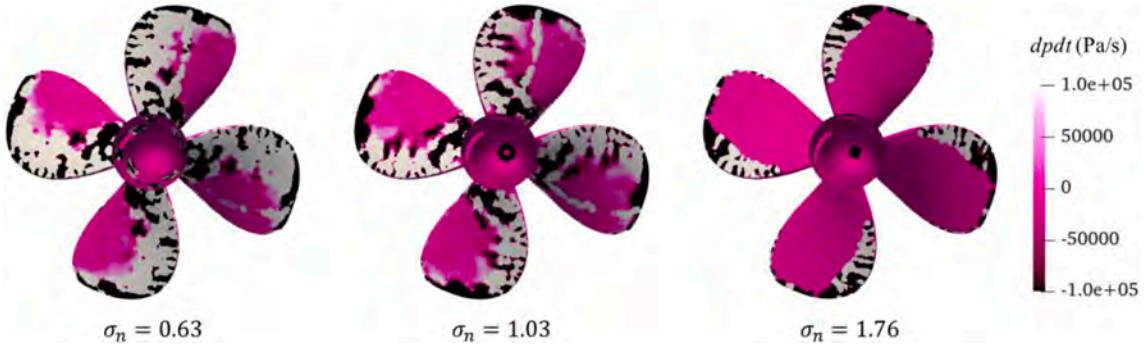


**Fig. 8.** The dipole source of different cavitation number on the suction side of propeller.

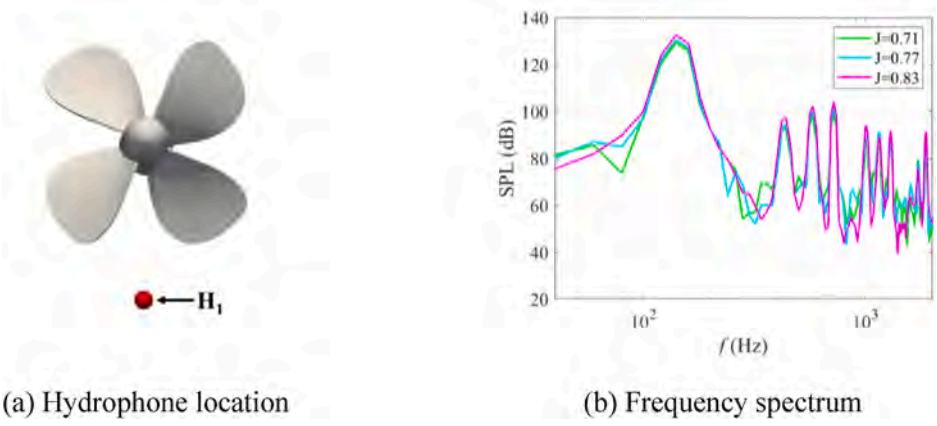


**Fig. 9.** The frequency spectrum of quadrupole results in different advance coefficients.

vector. $\dot{m}$ means the mass transportation between two phases. The purpose of cavitation model is to solve the problem of $\dot{m}$.

Schnerr deduced 'Schnerr-Sauer cavitation model' based on famous Rayleigh-Plesset equation (Schnerr and Sauer, 2001), which is

$$\dot{m} = \frac{\rho_l \rho_v}{\rho} \cdot \frac{3\alpha_v}{R} \cdot \sqrt{\frac{2}{3} \frac{|p_B - p_\infty|}{\rho_l}}$$

where $p_B$ is the internal pressure inside the cavity. $p_\infty$ means the external pressure. $R$ is the equivalent radius of bubbles. $\rho_l = 1000\text{kg/m}^3$ means the liquid density. $\rho_v = 0.023\text{kg/m}^3$ means the vapor density and $\rho = \alpha_l \rho_l + (1 - \alpha_l)\rho_v$. In practice, the process can be divided into vaporation ($\dot{m}_v$) and condensation ($\dot{m}_c$):

$$\dot{m}_c = C_c \frac{\rho_l \rho_v}{\rho} \cdot \frac{3\alpha_v}{R} \cdot \sqrt{\frac{2}{3} \frac{|p_B - p_\infty|}{\rho_l}}$$

$$\dot{m}_v = C_v \frac{\rho_l \rho_v}{\rho} \cdot \frac{3\alpha_v}{R} \cdot \sqrt{\frac{2}{3} \frac{|p_B - p_\infty|}{\rho_l}}$$

in which $C_c$ and $C_v$ are experiment coefficients.

### 2.3. Sound pressure prediction

For the underwater environment, the most common equation form is known as 'Farassat 1A Formulation', which is suitable for low Mach

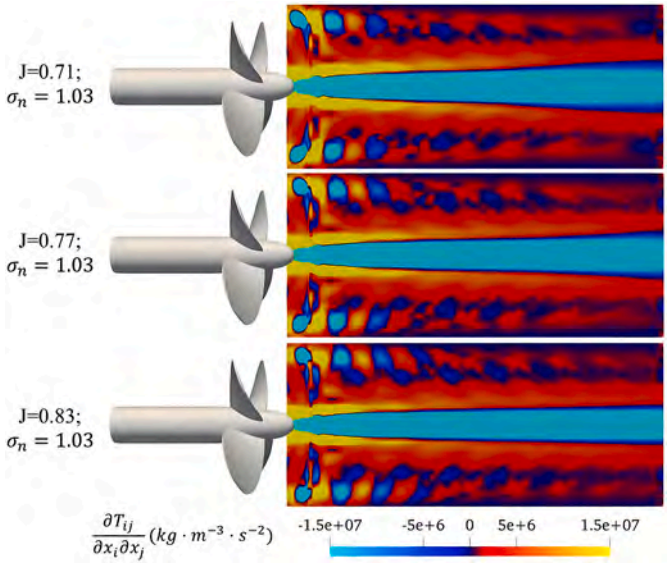


**Fig. 10.** The quadrupole source distribution of different advance coefficient on the $y = 0$ plane.

number conditions (Farassat and Brentner, 1998). It can be expressed like:

$$4\pi p_T'(x,t) = \int_{f=0} \left[ \frac{\rho_0 \dot{v}_n}{r(1-M_r)^2} + \frac{\rho_0 v_n \hat{r}_i \dot{M}_i}{r(1-M_r)^3} \right]_{ret} dS + \int_{f=0} \left[ \frac{\rho_0 c_0 v_n (M_r - M^2)}{r^2 (1-M_r)^3} \right]_{ret} dS$$

$$4\pi p_L'(x,t) = \int_{f=0} \left[ \frac{\dot{p}\cos\theta}{c_0 r(1-M_r)^2} + \frac{\hat{r}_i \dot{M}_i p \cos\theta}{c_0 r(1-M_r)^3} \right]_{ret} dS + \int_{f=0} \left[ \frac{p(\cos\theta - M_i \eta_i)}{r^2(1-M_r)^2} + \frac{(M_r - M^2) p \cos\theta}{r^2 (1-M_r)^3} \right]_{ret} dS$$

In these equations, $p_T'$ is monopole sound pressure, while $p_L'$ is dipole sound pressure. $(x,t)$ $(y,\tau)$ are space-time quantities for observer reference frame and source reference frame. $r = |x-y|$ means the vector between source and observer, while $\hat{r}_i = \frac{(x-y)}{r}$ is the normalized vector. $M_r = \frac{\hat{r} v_i}{c_0}$ is Mach number. $\dot{v}_n = \frac{\partial}{\partial \tau}(\vec{v} \cdot \vec{n})$ means the source time derivative of velocity. $\cos\theta = n_i \hat{r}_i$ is the angle cosine between the observer direction and source direction (source grid normal vector).

Farassat 1A Formulation shows the linear source terms. However, the quadrupole is not included in it. Strictly speaking, quadrupole sound pressure need volume integration. It is like:

$$4\pi p_Q'(x,t) = \frac{1}{c_0^2} \frac{\partial^2}{\partial t^2} \int_{f>0} \left\{ T_{ij} \left[ \frac{\hat{r}_i \hat{r}_j}{r^*} \right] \right\}_\tau dV + \frac{1}{c_0} \frac{\partial}{\partial t} \int_{f>0} \left\{ T_{ij} \left[ \frac{2\hat{r}_r \hat{r}_j^*}{r^*} + \frac{\hat{r}_i^* \hat{r}_j^* - R_{ij}^*}{\beta^2 r^{*2}} \right] \right\}_\tau dV + \int_{f>0} \left\{ T_{ij} \left[ \frac{3\hat{r}_i^* \hat{r}_j^* - R_{ij}^*}{r^{*3}} \right] \right\} dV$$

where $p_Q'$ is the quadrupole sound pressure and $T_{ij} = \rho u_i u_j$ simply. Other quantities' meaning are expressed in the literature (Cianferra et al., 2019).

As we all know, the volume integration is expensive. Here, the dual-mesh technology is adopted to improve the efficiency. It is realized by two meshes in the domain. One is the fluid mesh which is finer. The other is the acoustic mesh which is coarser. The acoustic mesh quantities are obtained by linear sum like

$$\phi_i^{acoustic} = \sum_{j=0}^{N_i} \varphi_{i,j}^{CFD} \cdot V_{i,j}^{CFD}$$

Here, $\varphi$ could be any quantity which is focused. The subscript $i$ means the $i^{th}$ acoustic grid, while $i,j$ means the $j^{th}$ fluid grid on the $i^{th}$ acoustic grid. $V^{CFD}$ is the volume of the fluid grid.

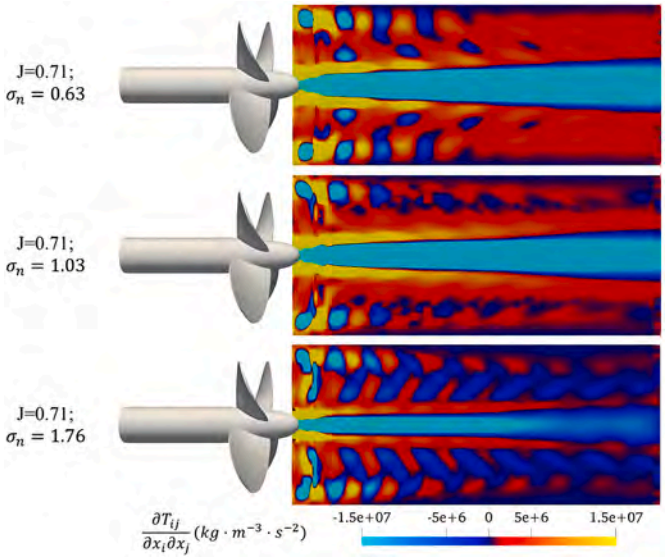


**Fig. 12.** The quadrupole source distribution of different cavitation number on the $y = 0$ plane.

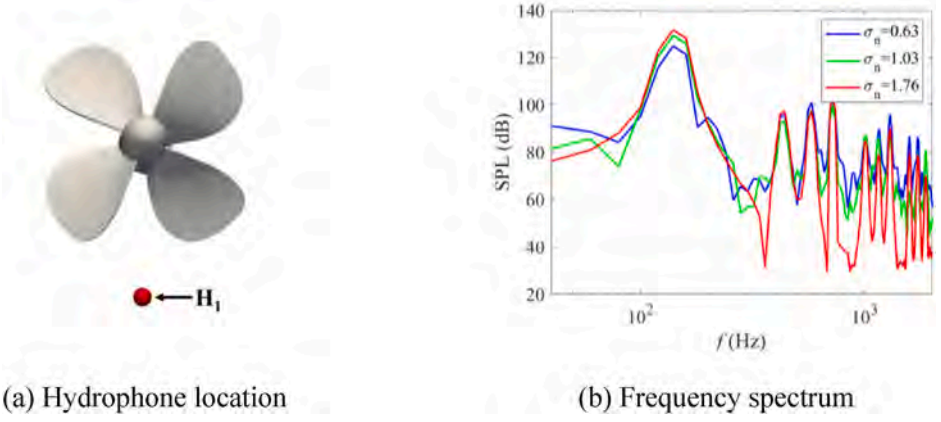


**Fig. 11.** The frequency spectrum of quadrupole results in different cavitation numbers.

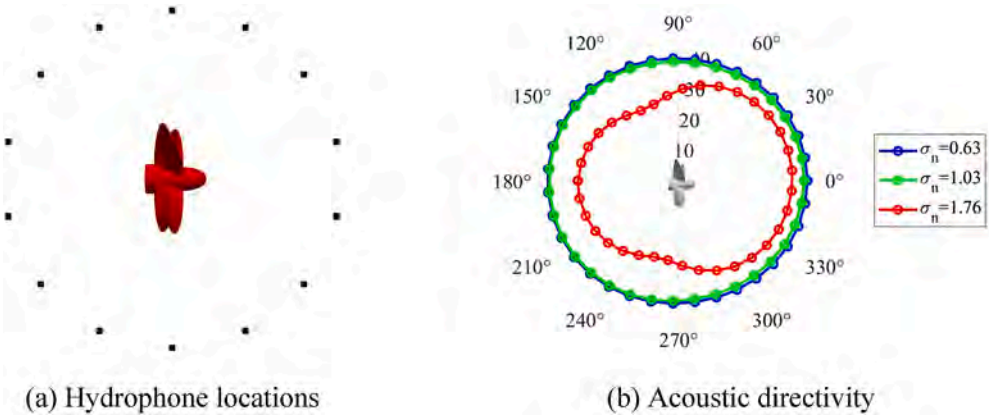


**Fig. 13.** The sound directivity of quadrupole results in different cavitation numbers.

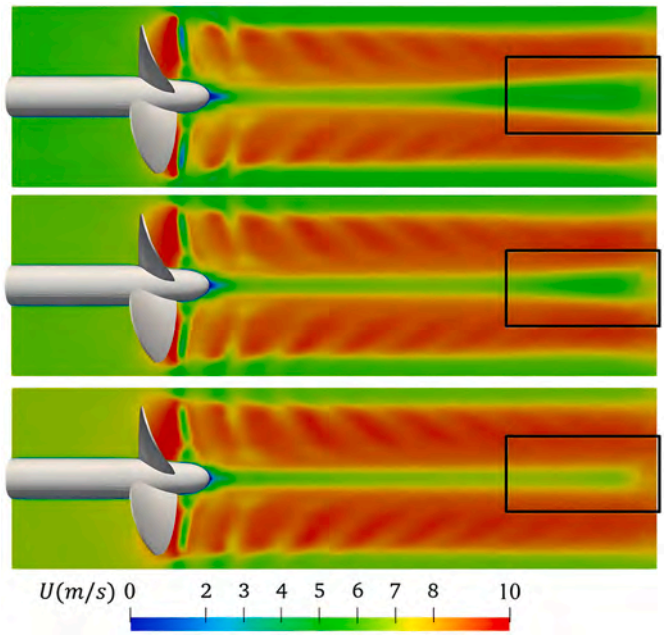


**Fig. 14.** The velocity slice with different cavitation numbers for INSEAN E779A propeller: NO.3 to NO.1 from top to bottom separately.

With the help of dual-mesh technology, the time delay effect can be added for quadrupole sound prediction. In the past studies, the time delay was often ignored. However, for those underwater problems with large scale source, little time steps and wide frequency bands, it should be considered. In the specific operation for this paper, it is computed as follows: First, the distance between the hydrophone and every source grid is calculated and stored. Then, the distance is divided by sound wave velocity ($c_0$) as the time delay. Finally, the receiver time is equal to the source time added by time delay. According to such rules, the sound pressure on each hydrophone is integrated at any receiver time.

For cavitation, another sound source caused by phase change need to be added. In this paper, it is formed as sphere source. The expression is like

$$p'_{cav}(\boldsymbol{x},t)=\frac{\dot{Q}(t-r/c_0)}{4\pi r}$$

In the formulation, there is

$$Q=\int qdV=\frac{d}{dt}(\rho V)$$

Where $p'_{cav}$ means the sound caused by cavitation or phase change. $q$ is density change. $V$ is cavity volume. $r$ is the distance between cavitation grid and receiver.

In the fellow parts, the sound pressure is computed by monopole, dipole, quadrupole and sphere four components. They are added together to obtain the total sound pressure.

### 2.4. Sound source extraction

In this paper, the sound source is divided into four parts: monopole, dipole, quadrupole and sphere source. According to Farassat 1A formulation, the monopole sound pressure $p'_T$ is related the normal velocity perpendicular to the object surface grid $v_n$ and its time derivative $\dot{v}_n$.

Focused on dipole $p'_L$, it is easy to find that dipole intensity is related to pressure $p$ and time derivative of pressure $\dot{p}$.

Quadrupole source is the space divergence of Lighthill tensor $\frac{\partial^2}{\partial x_i \partial x_j}(T_{ij})$. For high Renolds number and barotropic fluid, Lighthill tensor can be simplified as $T_{ij}=\rho u_i u_j$.

As for sphere source, the $p'_{cav}$ expressed in the form of phase fraction:

$$p'_{cav}(\boldsymbol{x},t)=\frac{\rho}{4\pi}\frac{\partial}{\partial t}\left[\frac{1}{r}\int_V \frac{\partial \alpha_V}{\partial t}dV\right]$$

where $\alpha_V$ is phase fraction of vapor.

## 3. Numerical setup and validation

### 3.1. Numerical setup

In this paper, INSEAN E779A (Italian Ship Model Basin) four-blade propeller is used as the research object for noise predictions. The experiment results of E779A propeller is detailed, especially for the cavitation flow field and underwater noise. It is a fixed-pitch, right-handed propeller designed in 1959. The propeller shape are shown in Table 1.

A cylinder-shaped domain is adopted, which is consistent with the experiment (Salvatore et al., 2006). The boundary conditions of the propeller surface and sidewall are set as no-slip. The propeller disk is located at a distance of 2.2D downstream from the inlet, and the outlet plane is 3.5D downstream of the disk surface. The diameter of the cylinder domain is 2.5D, to avoid the sidewall disturbance. The cylinder-shaped AMI (Arbitrary Mesh Interface) is 0.5D length from disk both upstream and downstream with a diameter of 1.2D. The volume-integration subrange covers a diameter of 1.25 D. Unstructured mesh is adopted near the propeller and structured mesh is for the rest of the domain. The WALE SGS model is used for LES. Schnerr-Sauer

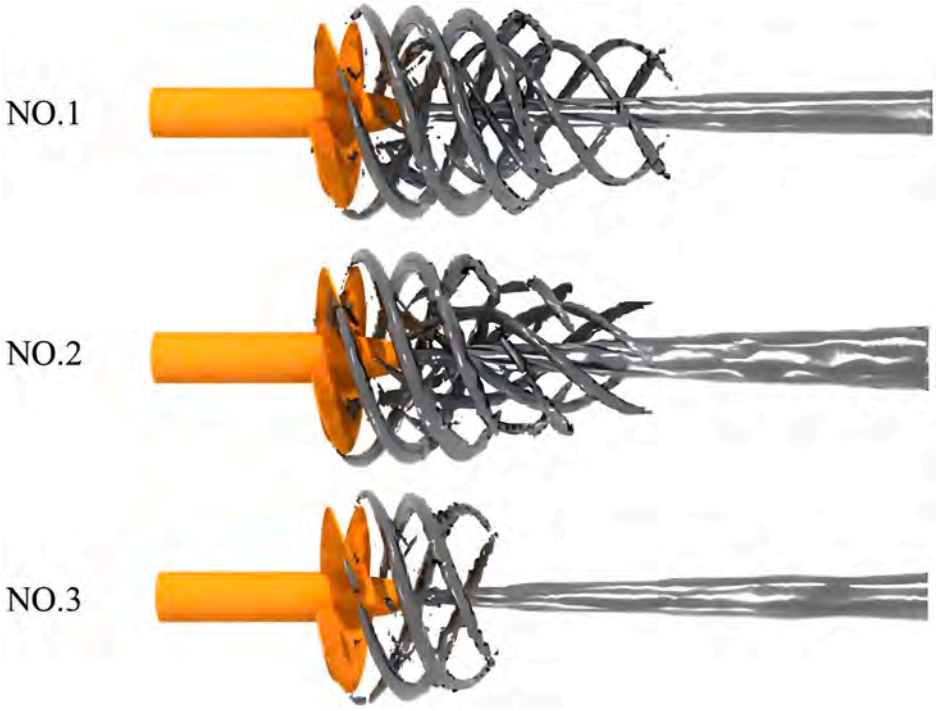


**Fig. 15.** The contour of vortex shedding in different cavitation number ($\Omega_R = 0.52$): $\Omega_R = \frac{\beta^2}{\alpha^2+\beta^2+\epsilon}$, where $\alpha = \frac{1}{2}\sqrt{\left(\frac{\partial v_Q}{\partial y_Q} - \frac{\partial u_Q}{\partial x_Q}\right)^2 + \left(\frac{\partial v_Q}{\partial x_Q} + \frac{\partial u_Q}{\partial y_Q}\right)^2}$ and $\beta = \frac{1}{2}\left(\frac{\partial v_Q}{\partial x_Q} - \frac{\partial u_Q}{\partial y_Q}\right)$ (Liu et al., 2018).

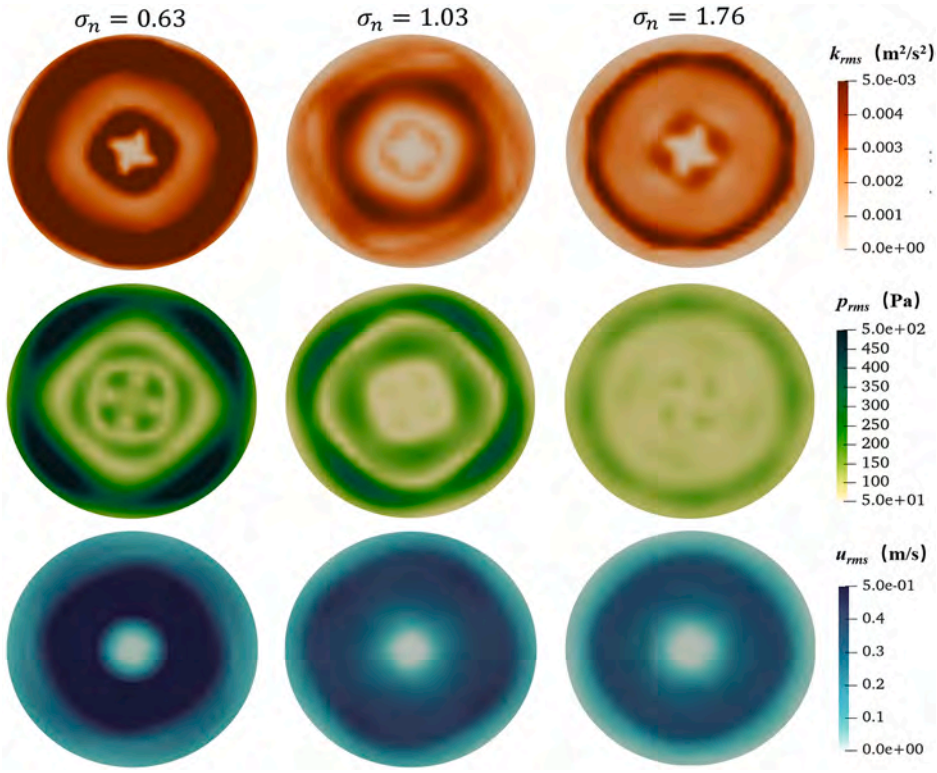


**Fig. 16.** The root mean square on the downstream slice in different cavitation numbers.

cavitation model is adopted, with the saturation pressure $p_v = 2300$ Pa, The density of water is set to 1000kg/m$^3$ while 0.023kg/m$^3$ for vapor.

The total number of grids is about 11 million. To make it easier to view the grid distribution, Fig. 1 shows the coarsened mesh. Unstructured grid is used around propeller; Structured grid is used in the far field.

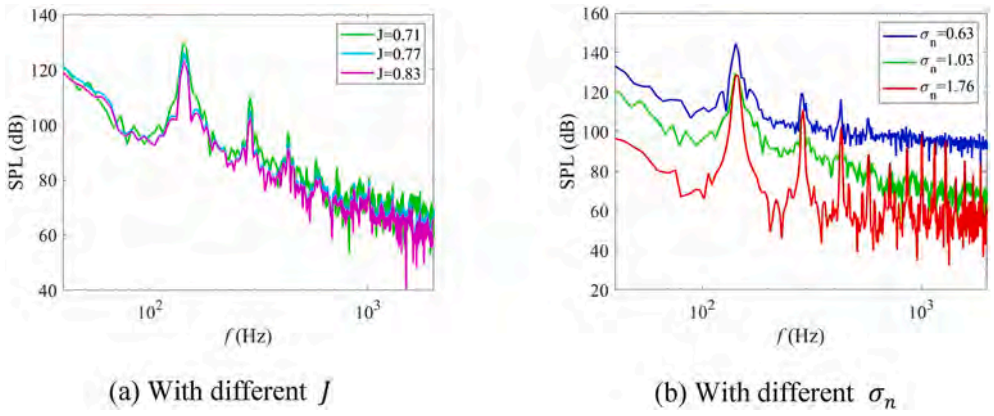


**Fig. 17.** The frequency spectrum of sphere results in different conditions.

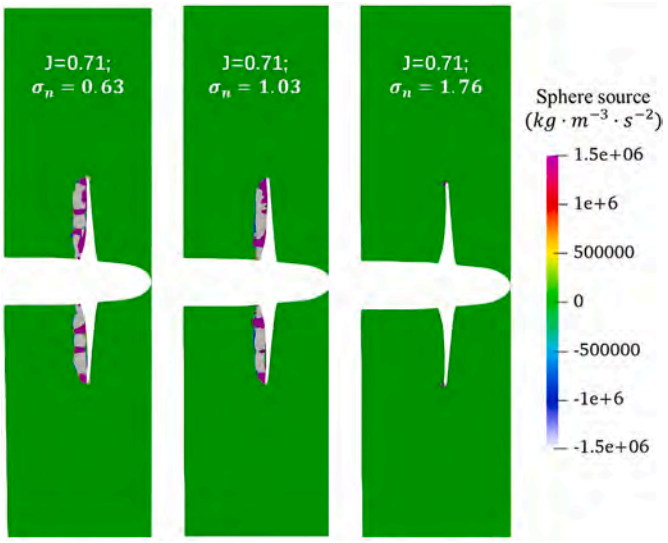


**Fig. 18.** The sphere source distribution of different cavitation numbers on the $y = 0$ plane.

To study the effects of advance coefficients $J$, cavitation numbers $\sigma_n$ and non-uniform inflow on the cavitation noise, six working conditions are selected, as is shown in Table 2. Among them, NO.6 stands for the non-uniform inlet condition, which is compared with the experiment.

An artificial wake generator is used to simulate non-uniform inflow conditions. Fig. 2 shows the generator shape and location. In the experiment, the device is 86 mm thick and 300 mm long. In the numerical simulation, the same size is adopted. The generator is 0.1 m away from the inlet surface. The incoming velocity of flowing is set $U_0$ = 6.22m/s, and the rotation speed is n = 30.5rps.

### 3.2. Numerical validation

After the calculation results are steady, NO.l, NO.3, and NO.5 conditions are selected for comparison with the experiment, as shown in Fig. 3. The numerical cavity snapshots are in the same view as the experiment pictures. The picture of the cavitation shown in Fig. 3 is stabilized by observation and corresponds to a physical time of 50 propeller rotation cycles, at which point statistics such as thrust, torque, and rms of the cavitation area have converged.

It can be seen that the simulation results are consistent with the experiments. It should be declared that some separated bubbles captured by the experiment cannot be simulated due to the limitation of the grid amount. However, according to the experience of hydrofoil cavitation noise, the cavitation noise is mainly related to the volume pulsation of the sheeted cavitation.

The quantitative comparison with the experiment measurements is also accomplished in the average number and standard deviation of cavitation area (in one rotation circle, about 0.0278s), as shown in Table 3. The latter lay the foundation for the subsequent sound source, because the sphere component is related to the cavity volume variation.

Furthermore, the non-uniform condition (Case NO.6) is verified, as

**Table 4**
The cavitation area of INSEAN E779A propeller for various cavitation numbers.

| Condition | $J$ | $\sigma_n$ | $\widehat{A}c/A_0$ |
|---|---|---|---|
| NO.1 | 0.710 | 0.63 | 1.416 |
| NO.2 | 0.710 | 1.03 | 0.809 |
| NO.3 | 0.710 | 1.763 | 0.269 |

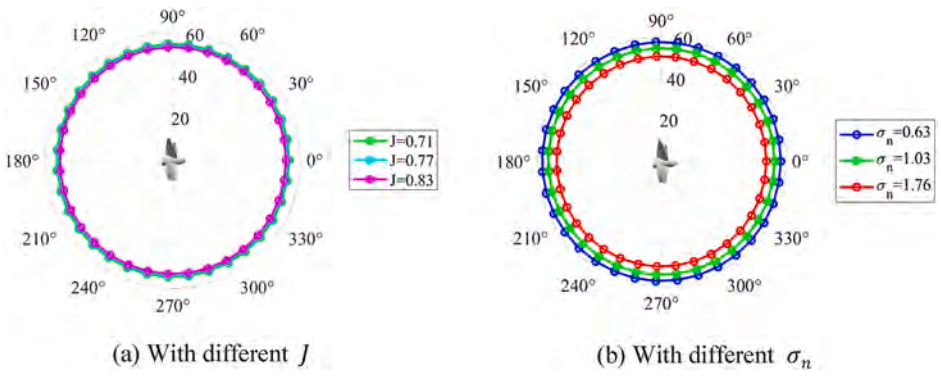


**Fig. 19.** The sound directivity of sphere results in different working conditions.

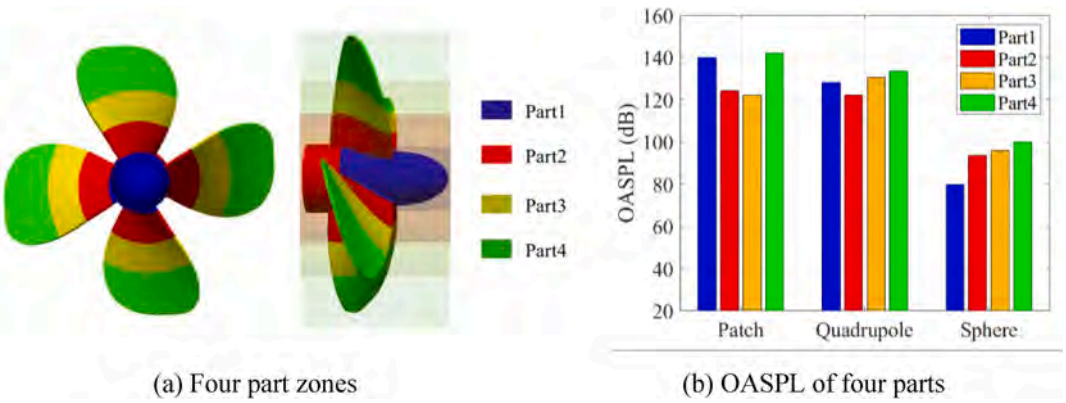


**Fig. 20.** The OASPL of different components in 4 parts for INSEAN E779A propeller.

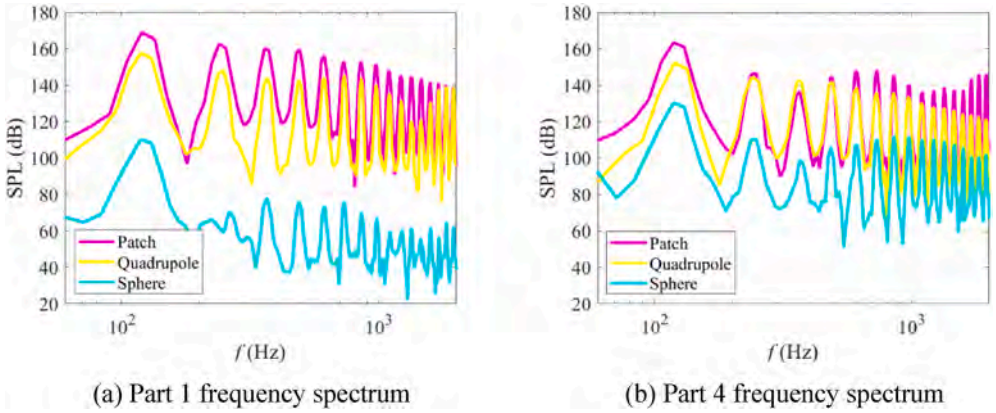


**Fig. 21.** The frequency spectrum of different components in 4 parts for INSEAN E779A propeller.

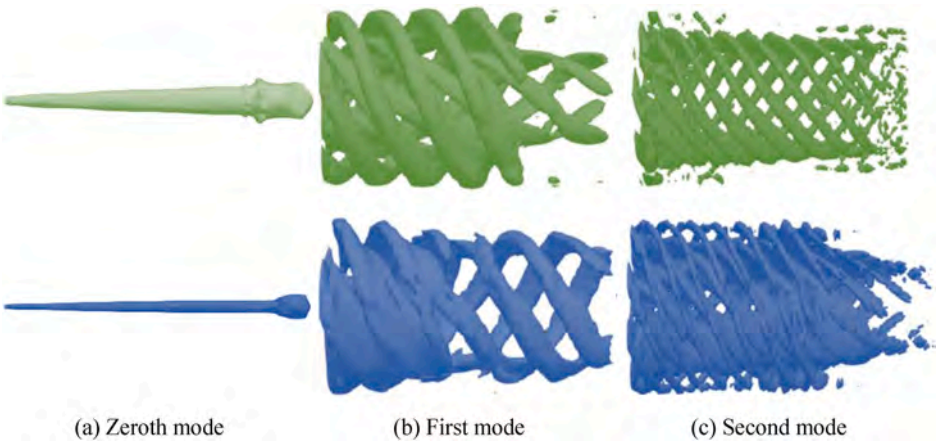


**Fig. 22.** The comparison of vortex shedding modes (Uniform one is in green and non-uniform one is in blue). (For interpretation of the references to color in this figure legend, the reader is referred to the Web version of this article.)

shown in Fig. 4. It can be seen that the two are similar. The cavitation area obtained by experiment is about 0.002968m$^2$, and that obtained by the simulation is about 0.0032m$^2$, with an error less than 8 %.

A near-field hydrophone, named $H_1$, is located as shown in Fig. 5(a). It is 0.5D downstream from the propeller disk, and the z-direction distances is 0.65D below the propeller, the same as the experiment. The noise prediction combines quadrupole and sphere sound source in volume integration, while monopole and dipole sound source is obtained by surface integration at the object surface. The dual-mesh technology is used to accelerate the volume integration. Fig. 5(b) shows SPLs of two mesh strategies. It can be seen that errors at the first four peak frequencies (120 Hz, 24 Hz, 360 Hz, and 480 Hz) are less than 6 dB.

The 1st peak SPL results with two mesh strategies are compared, and the errors are calculated referring to the experiment. Besides, the computation time are also collected to evaluate the efficiency improvement, as shown in Table 3. The error increases by about 1.8 dB using dual-mesh method. However, the computation time is reduced from 2408.8h to 386.5h.

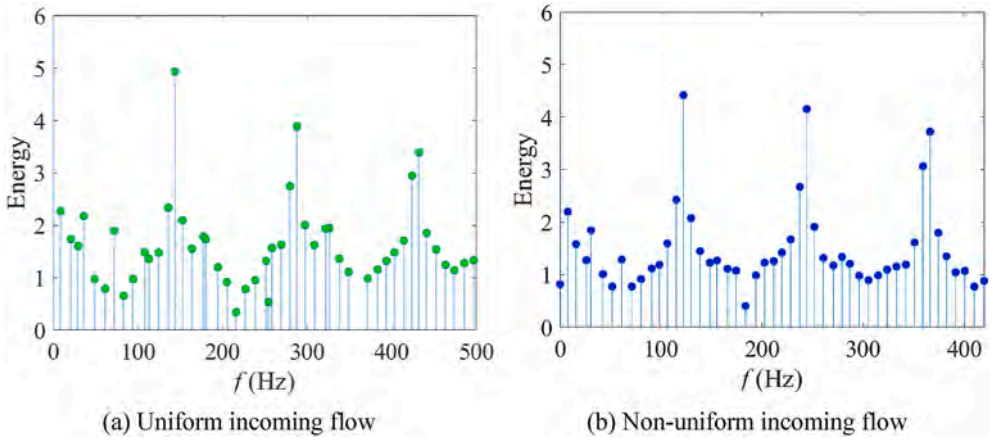


**Fig. 23.** The comparison of vortex shedding energy between uniform and non-uniform inlet.

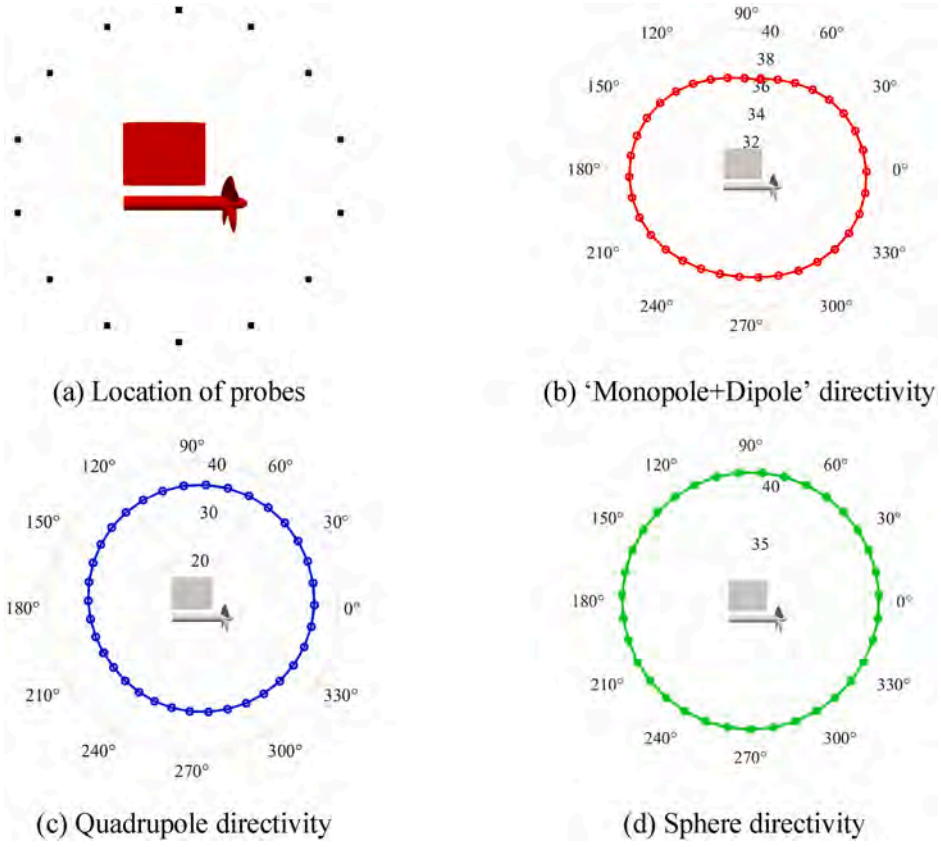


**Fig. 24.** The sound directivity of three acoustic components in non-uniform inlet flow.

## 4. The flow-sound correlation mechanism

### 4.1. On propeller side force

It has been proved (Keller et al., 2018) that the propeller side force has a greater effect on the noise than the thrust force. Therefore, it is addressed and analyzed in this subsection. The propeller cavitation noise can be divided into three parts: "monopole + dipole", "quadrupole" and "sphere" sound pressure. Their characteristics are analyzed separately. The part "monopole + dipole" is integrated by surface, so the two sources are summed up. Because the rotational speeds are identical, so there is no point in comparing the monopole individually. Quadrupole is a sound source caused by turbulent pulsation in the propeller wake, and spherical sound source is caused by cavitation phase change. These three sound source components have different acoustic mechanisms.

Fig. 6 shows the correlation coefficients between the propeller side force and the dipole sound pressure for the NO.2 case, with a hydrophone located 50D above the propeller. It can be seen that the correlation is high in the whole frequency band, indicating that the side force of the propeller has a large influence on the dipole sound pressure.

In order to investigate the acoustic directivity, a series of hydrophones are set around INSEAN E779A propeller. These probes are located in the $y = 0$ plane, centered on the propeller, with a radius of 50D every 10°, that is, there are 36 probes. The downstream direction is taken as 0°, and the z-axis positive direction is taken as 90°. The acoustic

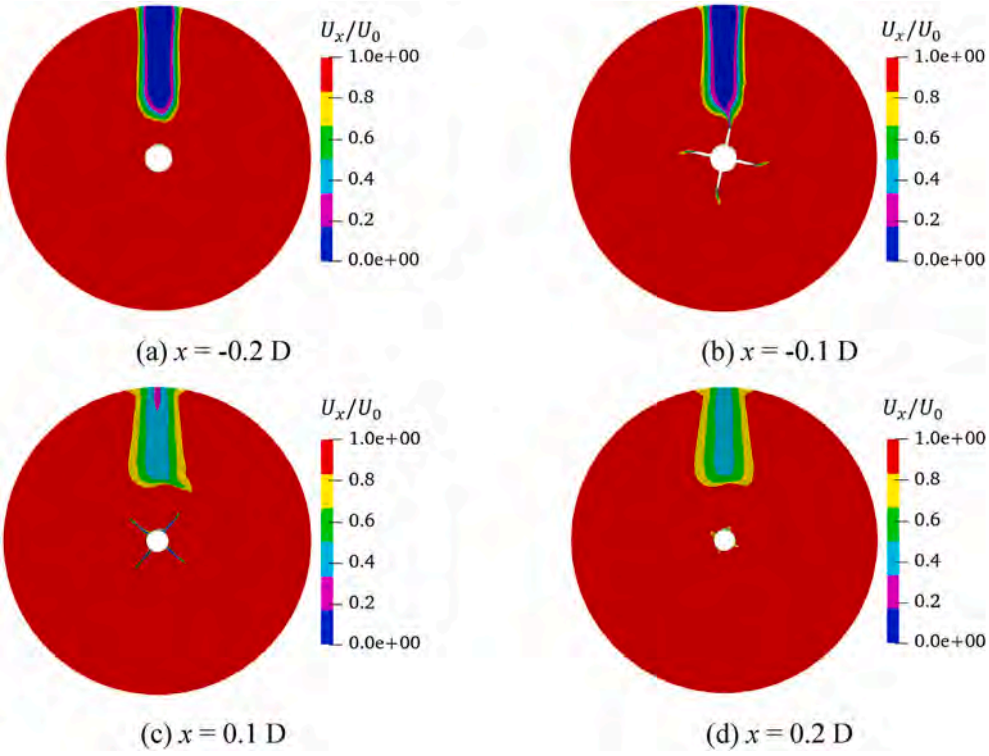


**Fig. 25.** The velocity distribution on different slice in non-uniform wake for INSEAN E779A.

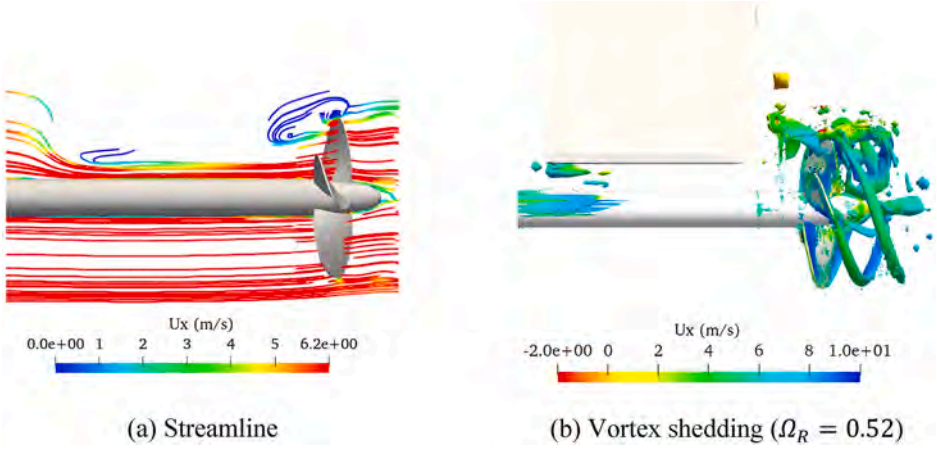


**Fig. 26.** The streamlines and vortex shedding in non-uniform wake for INSEAN E779A.

directivity of‘‘monopole + dipole’’ is shown in Fig. 7. It is characterized by ″∞” shape, with peak values in the upstream and downstream of the propeller. The OASPL increases with the increase of the advance coefficient, while decreases with the cavitation number.

This can be explained from the side force fluctuation of the propeller, whose distribution is replaced by the $dp/dt$ contribution, as Fig. 8 shows. The higher the cavitation degree, the more intense the phase transition occurs, the stronger the side force fluctuates.

### 4.2. On vortex shedding

Vortex shedding affects the quadrupole sound source mainly. The quadrupole sound spectrum is shown in Fig. 9 with different advance coefficients. It seems no distinct difference in the quadrupole sound pressure of different advance coefficients. The quadrupole source distribution is plotted in Fig. 10, proving the similar conclusion. This indicates that the inlet velocity does not play an essential role on the quadrupole sound pressure.

Different cavitation numbers are also studied in quadrupole components. As shown in Fig. 11, the first-order peak value decreases with cavitation numbers. As shown in Fig. 12, quadrupole source distributions in the y = 0 plane are different obviously. The lower the cavitation number, the higher the intensity of the quadrupole sound source. This may be related to the fact that the low cavitation enhances vortex shedding in the wake region.

The quadrupole acoustic directivity is given, as shown in Fig. 13. It can be seen that the peaks in the upstream and downstream directions are not symmetrical: The range in the downstream direction is wider and stronger.

The velocity distribution is heavily influenced by the propeller wake. The velocity slice is shown in Fig. 14. At first, the contour is almost perpendicular to hubs. As the wake moves downstream, it shows a

greater slope, caused by the shear flow between the blade tips and hubs. As the convective velocity decreases, the shear vortex diminishes, resulting in the velocity contour less distinct. As can be seen in Fig. 14, a more distinct wake profile in low cavitation number condition, resulting in a wider range of downstream acoustic directivity.

With the help of the third-generation vortex identification technique, the propeller wake vortex shedding is extracted, as Fig. 15 shows. The larger the cavitation number, the shorter the vortex shedding lasts downstream. This accords with the hydroacoustic conclusion. In Fig. 16, the downstream slices of three cavitation numbers are plotted, with the root mean square (RMS) of the turbulent kinetic $k_{rms}$, pressure $p_{rms}$ and velocity $u_{rms}$. It can be seen that the values are the largest and most widely distributed with the cavitation number 0.63, which explains why the NO.l quadrupole acoustic directivity has the widest lobe downstream.

### 4.3. On cavitation behavior

The cavitation behavior mainly affects the sphere sound source. Since the advance coefficient does not have a significant effect on cavitation, it does not influence the sphere sound pressure, as shown in Fig. 17(a). The hydrophone locations are the same as those shown in Fig. 11. It can be seen that the sound pressure has a narrower bandwidth near the peak than the other two components ('Monopole + Dipole' and Quadrupole). This is due to the fact that the monopole, dipole and quadrupole are all affected by the complex flow field nonlinearity, whereas the sphere sound pressure depends only on the volume change of the cavity. Therefore, its line-spectrum features are more notable.

As is shown in Fig. 17 (b), the sphere sound component dominates the low-frequency band noise, and its influence is much larger than that of the monopole, dipole and quadrupole. As cavitation number increases, the sphere sound magnitude decreases dramatically. The sphere source distribution in the $y = 0$ plane is shown in Fig. 18. Since the cavitation state studied in this paper is sheet cavitation, only the sphere source near the blade is focused here. It can be seen that the larger the cavitation number, the lower the degree of cavitation. As the sphere source is positively correlated with the change rate of cavity volume, the sphere sound pressure decreases with the increase of $\sigma_n$.

As for the far-field acoustic directivity, the sphere sound component exhibits radial symmetry features, as Fig. 19 shows. The amplitude is the same in all directions. Such shape is related to the random variation of the cavity areas through one circle. Consistent with the near-field conclusions, the advance coefficient influence is not significant. On the contrary, the cavitation number plays a significant role for sphere sound directivity.

As the cavitation number decreases, the phase changes more violently, causing the sphere OASPL increases. This can be proved from the cavitation area, as shown in Table 4. With the increase of $\sigma_n$, the standard deviation of the cavitation area ($\widehat{A}c$) decreases. This results in a gradual decrease in the sphere sound pressure.

### 4.4. On non-uniform incoming flow

In this section, the mechanism of non-uniform incoming flow on the cavitation propeller noise is analyzed in the case NO.6. To study the sound contributions of different propeller parts, the regions are divided into four parts in cylindrical forms, denoted as Part 1, Part 2, Part 3, and Part 4 respectively. Their diameters are 0.25D, 0.5D, 0.75D, and l.lD respectively, as is shown in Fig. 20 (a). The surface integration is used to compute 'monopole + dipole' sound pressure (replaced by 'Patch'), while the volume integration is for quadrupole sound pressure and sphere sound pressure.

Fig. 20 (b) shows the OASPL of three sound components for the four parts. It reveals a relationship that 'monopole + dipole' > quadrupole > sphere. However, it should be noted that the quadrupole sound pressure is already similar to the 'monopole + dipole' sound pressure around the blade tips (Part 4), and the amplitude of the sphere component is enhanced. For both the 'monopole + dipole' component and the quadrupole sound, it is the hub region (Part l) and the tip region (Part 4) that own the highest contributions. As for the sphere component, the dominance of the blade tip (Part 4) is obvious particularly, due to the fact that the cavitation area is concentrated on tips mainly. The presence of vortex shedding and side force fluctuation in the hub (Part l) and blade tip (Part 4) regions result in a larger contribution of 'monopole + dipole' as well as quadrupole sound pressure in these two regions. Therefore, the design of low cavitation noise propeller is focused on the hub and tips.[30][163]

The frequency spectrum curves of the hub and tip regions are given in Fig. 21. It can be seen that both the 'monopole + dipole' and quadrupole sound components exhibit obvious narrow-band characteristics than the uniform incoming flow. This can be explained from the dynamic mode decomposition results of the flow field.

The propeller wake vortices are decomposed by DMD, plotted by the third generation vortex identification technique. As is shown in Fig. 22, NO.4 and NO.6 case are selected for comparison, where the green coloring is uniform flow and the blue coloring is non-uniform flow. $0^{th}$ order mode cloud map is $\Omega_R = 0.7$ vortex iso-surfaces, 1st order mode is $\Omega_R = 0.5$ and 2nd order mode is $\Omega_R = 0.3$. It can be seen that the vortex decreases with the mode order.

The distribution area of the non-uniform incoming flow is stronger than that of the uniform incoming flow at the higher order modes. Fig. 23 compares the energy of different modes for the two incoming flows. It is clear that the non-uniform incoming vorticity is larger than the uniform conditions at higher modes ($\geq 2^{nd}$). Although the uniform inflow is stronger at 1st mode, it decays rapidly in the higher orders. In contrast, the non-uniform inflow decays slowly, resulting in a more pronounced higher order peak in sound pressure spectrum.

To study the acoustic directivity in non-uniform incoming flow conditions, 36 probes are arranged in the $y = 0$ plane with the center of the propeller and a radius of 50D, as is shown in Fig. 24.

Observing the 'monopole + dipole' acoustic directivity, in addition to the high-energy directions in upstream and downstream, there is another feature different from the uniform incoming flow: that is, the whole shape is shifted to the bottom, and the OASPL below is higher than that above propeller. The change of acoustic directivity can be explained from the perspective of flow field structure. Take velocity slices as an example, as is shown in Fig. 25. Due to the blocking effect of the wake generator, there is an obvious velocity defect region above, which couples with the rotational velocity and produces deformation when approaching the propeller. As for the slices downstream, the velocity defect region shrinks gradually. It is known that the lower the velocity, the smaller the $dp/dt$ term on the propeller surface, and the lower the dipole sound is. It is because the velocity defects above the disk surface shifts the dipole acoustic directivity below propeller.

Unlike the uniform incoming flow where the quadrupole directivity is shifted directly downstream,the non-uniform incoming quadrupole is concentrated in the direction above the propeller downstream. Fig. 26 (a) gives the streamline near the propeller in the $y = 0$ slice. It can be seen that, due to the blocking effect of the wake generator, there exists a backflow at the blade upper tips, where the velocity decreases and the kinetic energy is weakened, causing the non-uniform incoming dipole directivity to be shifted toward the propeller downward. At the same time, some vortices appear behind the wake generator, which interacts with the propeller vortex shedding to form an asymmetric flow structure, as shown in Fig. 25(b). It is the existence of the vortex behind the wake generator that shifts the center of the quadrupole sound source distribution above the propeller, resulting in an upward shift of quadrupole directivity.

## 5. Summary and conclusions

In this paper, the flow field of INSEAN E779A cavitation propeller is simulated. Based on this, the mechanism of flow-sound correlation of cavitation propellers is investigated by using the dual-mesh technology with quadrupole and sphere source. The overall content is divided into three parts. One is the method description. The second part is the validation for the accuracy and efficiency. And the last part is the flow-sound correlation mechanism. The conclusions are obtained as follows:

The cavitation model and sliding mesh technique are introduced. On the basis of dipole extraction, the extraction of sphere source caused by phase change and monopole sound source caused by propeller rotation are added. Besides, the quadrupole extraction needs to take density variation and dual-mesh technology into consideration. For the flow-sound correlation study, three numerical tools are introduced: cross spectrum analysis, the third-generation vortex identification technique, and dynamic mode decomposition.

As for the validation, the numerical cavitation snapshots in uniform inflow conditions are compared with the pictures taken in the experiments, and the results are consistent with each other. The error of the sound pressure level is less than 6 dB at the first 4 peaks. Even though dual-mesh technology is adopted, the error increases less than 1.8 Db. However, the computation time is shortened from 2408.8 h–386.5 h, with a 6.23 times improvement in efficiency.

The correlation between the propeller side force and the dipole sound is high in all frequency bands, and the advance coefficient affects the dipole by influencing the side force. The lower the cavitation number, the higher the surface force fluctuation, which is reflected in the increased dipole intensity. The vortex affects the turbulence in the wake region, which contributes to the quadrupole source. The vortex shedding lasts longer, the flow fluctuation is larger, and the quadrupole in the downstream direction is also wider and stronger. The cavitation behavior affects the sphere pressure. The smaller the cavitation number and the larger the standard deviation value of the cavitation area, the stronger the sphere source is. The monopole, dipole and quadrupole sound components under non-uniform inflow conditions all exhibit more pronounced narrow-band peaks than those of uniform inflow. DMD results of the propeller wake vortices reveals that the uniform inflow, despite its higher energy at the 1st order mode, decays rapidly at higher order modes. While the non-uniform inflow decays slower, resulting in more pronounced peaks at the higher order frequencies. In addition, the presence of velocity defects above the disk surface shifts the dipole acoustic directivity below propeller. At the same time, the quadrupole acoustic directivity is shifted upwards.

## CRediT authorship contribution statement

**Lianjie Yu:** Writing – original draft, Visualization, Validation, Software, Methodology, Investigation, Data curation. **Decheng Wan:** Writing – review & editing, Supervision, Funding acquisition, Conceptualization. **Yan Gao:** Investigation. **Qi Shen:** Software. **Shang Shi:** Validation. **Jiaao Geng:** Visualization.

## Declaration of competing interest

The authors declare that they have no known competing financial interests or personal relationships that could have appeared to influence the work reported in this paper.

## Acknowledgement

This work was supported by the National Natural Science Foundation of China (52131102), to which the authors are most grateful.

## Data availability

The data that support the findings of this study are available from the corresponding author upon reasonable request.

## References

Bosschers, J., 2018. A semi-empirical prediction method for broadband hull-pressure fluctuations and underwater radiated noise by propeller tip vortex cavitation. J. Mar. Sci. Eng. 6 (2), 49.
Cianferra, M., Ianniello, S., Armenio, V., 2019. Assessment of methodologies for the solution of the Ffowcs Williams and Hawkings equation using LES of incompressible single-phase flow around a finite-size square cylinder. J. Sound Vib. 453, 1–24.
Farassat, F., Brentner, K.S., 1998. The acoustic analogy and the prediction of the noise of rotating blades. Theor. Comput. Fluid Dynam. 10 (1), 155–170.
Keller, J., Kumar, P., Mahesh, K., 2018. Examination of propeller sound production using large eddy simulation. Physical Review Fluids 3 (6), 064601.
Lidtke, A.K., Humphrey, V.F., Turnock, S.R., 2016. Feasibility study into a computational approach for marine propeller noise and cavitation modelling. Ocean Eng. 120, 152–159.
Liu, C., Gao, Y., Tian, S., et al., 2018. Rortex—A new vortex vector definition and vorticity tensor and vector decompositions. Phys. Fluids 30 (3).
Nicoud, F., Ducros, F., 1999. Subgrid-scale stress modelling based on the square of the velocity gradient tensor. Flow Turbul. Combust. 62 (3), 183–200.
Noughabi, A.K., Bayati, M., Tadjfar, M., 2017. Investigation of cavitation phenomena on noise of underwater propeller. In: Proceedings of the ASME 2017 Fluids Engineering Division Summer Meeting, Waikoloa, Hawai'I, vol. 10.
Posa, A., Felli, M., Broglia, R., 2022. The signature of a propeller–rudder system: acoustic analogy based on LES data. Ocean Eng. 259, 112059.
Salvatore, F., Pereira, F., Felli, M., et al., 2006. Description of the INSEAN E779A propeller experimental dataset[R]. Technical Report INSEAN 2006-085 INSEAN-Italian Ship Model Basin.
Schnerr, G.H., Sauer, J., 2001. Physical and numerical modeling of unsteady cavitation dynamics[C]. In: Fourth International Conference on Multiphase Flow, vol. 1. ICMF New Orleans, New Orleans, LO, USA.
Sezen, S., Kinaci, O.K., 2019. Incompressible flow assumption in hydroacoustic predictions of marine propellers. Ocean Eng. 186, 106138.
Smagorinsky, J., 1963. General circulation experiments with the primitive equations: I. The basic experiment. Mon. Weather Rev. 91 (3), 99–164.
Zhao, W., Zhou, F., Fan, G., 2023. Assessment of subgrid-scale models in wall-modeled large-eddy simulations of turbulent channel flows. J. Hydrodyn. 35 (3), 407–416.
Zhu, W., Gao, H., Song, Y., 2017. Numerical investigation of propeller noise from tip vortex cavitation. Int. Conf. Offshore Mech. Arctic Eng. 57748, V07BT06A046. American Society of Mechanical Engineers.